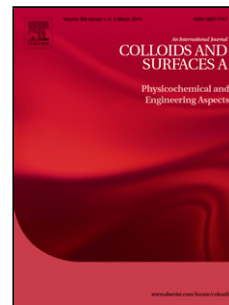


Accepted Manuscript

Title: Engineering microscale two-dimensional gold nanoparticle cluster arrays for advanced Raman sensing: an AFM study

Author: F. Domenici C. Fasolato E. Mazzi L. De Angelis F. Brasili F. Mura P. Postorino F. Bordi



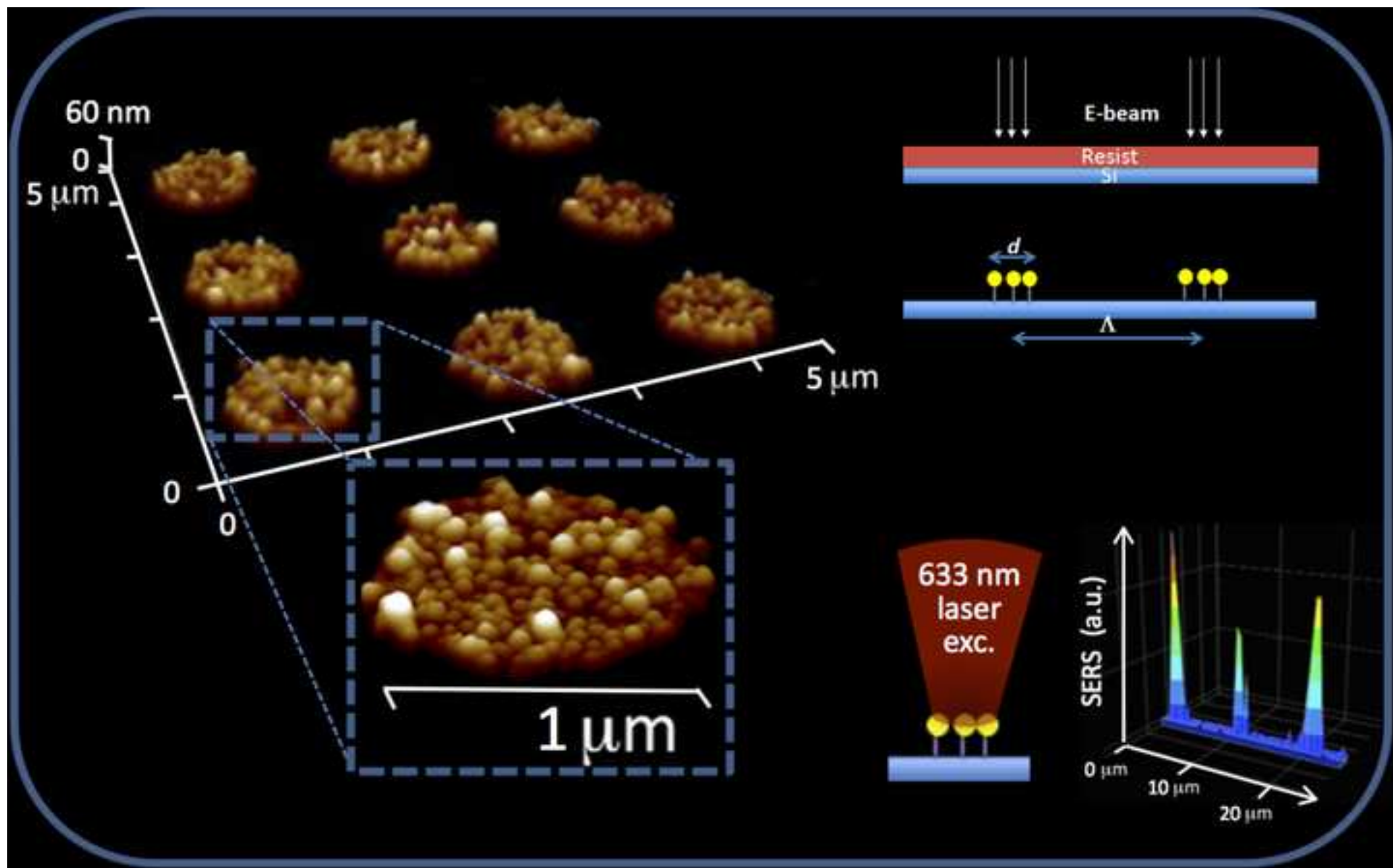
PII: S0927-7757(16)30185-6
DOI: <http://dx.doi.org/doi:10.1016/j.colsurfa.2016.03.043>
Reference: COLSUA 20524

To appear in: *Colloids and Surfaces A: Physicochem. Eng. Aspects*

Received date: 10-12-2015
Revised date: 13-3-2016
Accepted date: 14-3-2016

Please cite this article as: F.Domenici, C.Fasolato, E.Mazzi, L.De Angelis, F.Brasili, F.Mura, P.Postorino, F.Bordi, Engineering microscale two-dimensional gold nanoparticle cluster arrays for advanced Raman sensing: an AFM study, *Colloids and Surfaces A: Physicochemical and Engineering Aspects* <http://dx.doi.org/10.1016/j.colsurfa.2016.03.043>

This is a PDF file of an unedited manuscript that has been accepted for publication. As a service to our customers we are providing this early version of the manuscript. The manuscript will undergo copyediting, typesetting, and review of the resulting proof before it is published in its final form. Please note that during the production process errors may be discovered which could affect the content, and all legal disclaimers that apply to the journal pertain.



Highlights

- Design and AFM analysis of nanoparticle cluster arrays for improved Raman sensing
- Electron beam lithography templates were optimized by varying the e-beam dose
- Tightly packed and regularly shaped 2D gold nanoparticle assemblies were reached
- The microsized clusters provided a huge and reproducible gain of the Raman signal

Abstract

We realized and tested a strategy for developing reproducible and stable two-dimensional gold nanoparticle cluster arrays arranged on silicon substrates, to be used for surface-enhanced Raman spectroscopy. We combined electron beam lithography and molecular functionalization to finely control the shape of the nanoparticle assemblies. Atomic force microscopy analysis allowed to optimize the procedure of nanoparticle cluster array fabrication in terms of electron beam dose and chemical protocol, enabling to achieve a good regularity in spacing and size (i.e. area and layer number) of the clusters. MicroRaman space resolved measurements were undertaken on large 2D arrays ($100\times 100\ \mu\text{m}^2$) made up of regularly microsized clusters. The high surface enhanced Raman signal measured on the structures highlights the full correspondence of the spatial and optical periodicity achieved. This standardized procedure represent the basis to realize versatile platforms for nano-optical investigation and towards an efficient high-sensitive multiplex sensing.

Keywords—AFM; nanoparticle clusters; array; EBL; surface-enhanced Raman scattering

1 **1. Introduction**

2 An important challenge for nanosensing investigation is the design of improved tools to overcome
3 uncertainties and shortcomings of current diagnostics [1-5]. This goal can be concretized realizing
4 ultrasensitive and molecular specific detection substrates using gold nanoparticles (NPs) [2-6]. The
5 rationale of the gold NPs choice lies in their peculiar properties of a high surface-to-volume ratio, the
6 possibility of suitable biomolecular conjugation [7-9], their rewarding chemical stability [7-9], and the
7 collective electronic behavior at their surface [10,11]. In particular, their electromagnetic signal
8 enhancement capability [10-12], combined with their ability to form hybrid assemblies with biomolecules
9 [3,4,8], provides the basis to probe molecular structures and conformation of biomolecules at
10 extraordinarily low concentration with spectroscopic tools. In this frame, we previously enlightened [13]
11 the role of spontaneous mesoscopic architectures, (NP clusters self-assembled on solid supports), in
12 providing a huge and size dependent enhancement of the Raman signal of the analyte confined within.
13 Analogously to single plasmonic objects, close packed NP aggregates can induce the confinement of
14 intense electromagnetic fields at their surface [13]. The Raman scattered intensity increases linearly with
15 the NP cluster area (up to $\sim 30 \mu\text{m}^2$), exhibiting different slopes depending on the aggregate thickness.
16 Such dependence on the thickness, allows to ascribe the increased variability of the Raman intensity
17 observed in larger clusters to their intrinsically higher inhomogeneity (variability of layer number)
18 [13,14]. These findings suggest that ordered, closely packed single layered "patches" of NP measuring a
19 few squared microns could guarantee an easy recognition of these aggregates within the optical resolution
20 of a microoptical apparatus, a good enhancement of the Raman signal, and a reduced Raman intensity
21 variability [3,15,16]. However, although micrometric fractal assemblies are easy and economical to
22 generate, the reproducibility of the giant Raman scattering enhancements are difficult to control in such
23 completely random structures.
24 Colloidal NPs can be assembled into deterministic arrays using top-down lithographic methods with
25 excellent reproducibility, such as focused ion beam techniques or Electron Beam Lithography (EBL)

1 [17,18]. The latter has recently emerged as a flexible and quick tool for extensive nano- and micro-
2 patterning, avoiding effects of ion implantation in exposed sites [17]. Unfortunately to date, it remains
3 tricky to generate NP sites with gaps of less than a few tenths-nm, with the disadvantage that the Raman
4 intensities arising from the so obtained architectures is significantly smaller than those achieved in
5 "chemically" assembled clusters of nearly touching NPs [6]. Consequently, rational nanofabrication
6 methods have to be tailored to create some challenging molecular and microorganisms sensing platforms
7 made up of strongly coupled NP clusters of well defined microscale area and morphology [16].

8 Proceeding from this, we combined EBL and self-assembly strategies [19-21] to develop novel two-
9 dimensional arrays of mesoscopic NPs aggregates with well-defined shape yielding a well-predictable
10 Raman field enhancement. Template guided self-assembly can in fact induce gold NP aggregation in
11 different, regular Nanoparticle Cluster Arrays (NCA) platforms, very promising for applications, where
12 the reproducibility of the clustered NP patches in terms of shape, size and thickness is crucial for their
13 optical response. In addition, the flexibility of the NCA fabrication approach makes it straightforward to
14 adjust the electromagnetic response of NCAs, varying the value of the characteristic parameters
15 [3,15,16,22].

16 Within these purposes, the first step in NCA fabrication is optimizing the electron beam (e-beam) dose
17 value with respect to the reproducibility of the mask geometry involved. There is a trade-off among
18 speed, complexity and accuracy in the EBL writing of a desired mask. High energy e-beam is used for
19 optimal resolution, although electron scattering limits its application, particularly due to the "proximity
20 effect", where electrons writing a feature at one location overexpose a nearby feature, affecting the
21 pattern geometry [23,24]. The second necessary step is to frame the chemical derivatization strategy of
22 the EBL patterned surface in order to assure a selective and tight covering of the NPs (60 nm sized) on
23 the printed pattern.

24 The mesoscopic size of the cluster composing our NCA allows an easy determination of their position
25 by optical imaging. However, in order to gain detailed information on the shape of the patches and their

1 ordering and thickness we performed an accurate Atomic Force Microscopy (AFM) analysis. The optical,
2 microRaman and AFM combined imaging on the NCA functionalized with a Raman marker show an
3 excellent correspondence between the optical and the topographic array maps. The high enhancement
4 factor and the quite good reproducibility of the Raman sensing are promising for the implementation of
5 multiplexed sensing on this kind of substrates. Indeed, the regular, geometrical 2D disposition of the
6 clusters on the substrate allows to perform multiple measurements on a single sample, with the possibility
7 of a careful statistical analysis of the collected data. Moreover, the nature of the substrate paves the way
8 for the implementation of multiplexed sensing platform.

10 **2. Experimental**

11 *2.1. Electron Beam Lithography Setup*

12 EBL was performed using a Zeiss Auriga 405 Field Emission Microscope equipped with a Raith Elphy
13 Quantum EBL module (c/o SNN-Lab - Sapienza Nanoscience & Nanotechnology Lab). Before starting
14 the lithographic process, (100)-oriented silicon wafers were cleaned in absolute ethanol (organic cleaning)
15 and then sonicated (mechanical cleaning) for 2 minutes. Afterwards the wafer was placed in boiling 1,1,1-
16 Trichloroethane for 10 minutes and rinsed with milli-Q water. The treatment with an oxidizing solution
17 increases the number of the exposed Si-OH bonds, involved in the linkage with NPs, on the wafer
18 surface. The positive resist AR P632.04 (purchased from ALLRESIST GmbH, Germany) was employed
19 to obtain a silicon-supported poly-methylmethacrylate (PMMA) film through the spin-coating technique.
20 After several preliminary tests we established a working protocol, with a spin rate of 3000 r.p.m., that
21 ensures the deposition of a thin and uniform solid PMMA layer. After the resist coating, the sample was
22 baked in the oven at 120°C for 1 hour. This thermal annealing procedure stabilizes the film structure
23 cross-linking the chemical groups, removes the residual solvent, and the stress built up in the resist during
24 the spinning session [25]. The Atomic Force Microscopy (AFM) profilometry evaluated an almost
25 constant resist thickness of ~60 nm (see also Section 3.1). This steady thickness guarantees an accurate

1 lithography with a regular and well-defined micro-patterning of the substrate. Being the thickness of the
2 written PMMA comparable or smaller (Fig. S1a, b and c) than the NPs diameter, once the substrate has
3 been developed the surface functionalized and the particles deposited, the particles protrude partially out
4 of the well above the PMMA surface. In this way, measuring the AFM profiles, we were able to
5 investigate in details, the effective immobilization and the packing of the NPs on the masked resist
6 surface, and therefore the reproducibility of the whole substrate fabrication procedure.

7 The layout of the desired pattern was designed using the Computer-Aided Design (CAD) program of the
8 EBL module. On each sample, several pattern configurations (or sectors) were realized, varying the
9 diameter of the binding sites, d , and their periodical separation, Λ . The working parameters used were
10 step size and line spacing of 24 nm, dwell time of $6 \cdot 10^{-4}$ ms and two different area dose values (100
11 $\mu\text{C}/\text{cm}^2$ and $20 \mu\text{C}/\text{cm}^2$). The dose is defined as the product of beam current and beam dwell time, that is
12 the time taken for the electrons to penetrate the resist.

13 The e-beam exposed substrates were then treated with the developer AR 600-55 (ALLRESIST GmbH,
14 Germany) for 60 seconds, to favour a high solubility of the resist areas impinged by the e-beam. The
15 substrates were then transferred into the stopper bath AR 600-60 (ALLRESIST GmbH, Germany) for 30
16 seconds. This solution interrupted the development process and lead to a rapid rinsing of the residual
17 developer. Then, the substrates were rinsed in Milli-Q water and dried. After the development, the
18 substrates were baked again for 30 minutes to thermally anneal the exposed regions, in order to reduce
19 unwanted chemical changes within the resist layer during the exposure [25].

20

21 *2.2 NP Cluster Formation*

22 Gold NCAs were fabricated by a chemical bonding driven self-assembly of gold NPs, purchased from
23 Ted Pella, Inc., into the designed binding sites. The bare silicon surface of the lithographed substrate was
24 functionalized to allow the chemical binding of the NP to the surface. The functionalization of the silicon
25 surface was realized using two different protocols.

1 In the first protocol, the lithographed substrates surface were derivatized with 3% organosilane 3-amino-
2 propyltriethoxy-silane (APTS) solution in ethanol for 90 minutes at room temperature. The modified
3 plates were thoroughly rinsed with ethanol, baked at 110 °C for 10 minutes to stabilize further the
4 silanized silicon silane, and then reacted with 1% glutaraldehyde (Glu) solution for 30 minutes at room
5 temperature [25]. After thoroughly rinsing with milliQ water, the aldehyde-modified surfaces were
6 conjugated with the Raman active heterobifunctional crosslinker 4-aminothiophenol (4-ATP) [4] in water
7 solution (0.05 g/l 4-ATP) for 1 hour and then rinsed. Free thiol moieties were thus available to covalently
8 bind the NPs on the exposed silicon surfaces and the nanostructures was thus realized. Notice that the
9 APTS—Glu linker was successfully adopted also to build up sensitive and stable Raman biosensing
10 platforms in air and water environments [4].

11 In the second protocol, the thiols-driven stable connection between the bare gold NP surface and the
12 silicon substrates was instead promoted directly by using a 3-mercapto-propyltriethoxy-silane (MPTS).
13 The silicon substrates were incubated with 3% MPTS solution in ethanol for 90 minutes, and thus rinsed
14 and backed, according to the first protocol.

15 In both cases, NP incubation was performed with consecutive steps of NP deposition (at 25°C, for at least
16 3 hours) and thorough rinsing in milli-Q water, to ensure a high NP density to be connected at the silicon
17 surface, covalently. After each rinsing step the samples were dried under pure nitrogen gas. At the end of
18 the treatment they were stored in the refrigerator (at 4 °C). If not specified otherwise, the chemicals were
19 purchased from Sigma-Aldrich at analytical grade. Each step of the preparation was checked by AFM
20 (see Section 3).

21

22 2.3. AFM Measurements

23 Tapping-mode AFM images, using a cantilever with a spring constant, k , of 42 N/m, a scan rate of 0,3-0,7
24 Hz and an extremely sharp tip (nominal radius of curvature of 2 nm), were recorded by an Atomic Force
25 Microscope Dimension Icon Bruker (c/o SNN-Lab - Sapienza Nanoscience & Nanotechnology Lab). All

1 the AFM images shown herein are accompanied with a colour bar indicating the Z-range (height) of the
2 features on the sample. Data analysis was performed by NanoSope Analysis Version 1.4 (Bruker
3 Corporation).

4

5 *2.4 Raman Measurements*

6 For the Raman spectroscopy investigation, the surface of the NCAs obtained by both the protocols were
7 Raman-labelled with 4-ATP probe (Sigma-Aldrich) through a three hours incubation with a 0.05 g/l water
8 solution of the molecule, followed by Milli Q water rinsing to remove the unbound molecules, and drying
9 under pure nitrogen gas [5]. Raman measurements were performed with a LabRam HR Evolution Horiba
10 Scientific, using a 100× long working distance objective (N.A.=0.80) for the confocal microscope.
11 Surface Enhanced Raman Scattering (SERS) excitation was obtained with the 632.8 nm line of a He-Ne
12 laser. The spectrometer was equipped with an automatic mapping stage with submicrometric precision.
13 The spectroscopic images (SERS intensity maps) were obtained by collecting spectra at different,
14 regularly disposed positions on the sample, whose control was allowed by the microscope coupled with
15 the spectrometer. The step of the spectroscopic mapping was of 0.5 μm. The intensity of a selected
16 Raman/SERS band was then calculated by integrating the spectrum around the band frequency and
17 plotted against the spatial coordinates. The spectra were elaborated using LabSpec 6 and OriginPro 8
18 softwares and are herein presented without modifications. For the analysis of the intensity maps, a
19 polynomial baseline (3rd degree) was subtracted to the spectra before their integration.

20

21 **3. Results and discussion**

22 Several samples were prepared according to the protocol described in detail in Section 2, and schematized
23 in **Fig. 1**. Briefly, EBL was applied on a thin layer of a positive resist laid on flat hydrophilic silicon
24 surfaces (**Fig. 1a**). After the developing process, the exposed silanol surface was functionalized (**Fig. 1b**)

1 to allow the NPs confinement onto the designed circular well areas at a fixed diameter d and periodical
2 center-to-center spacing Λ (**Fig. 1c**).

3 In this section, we first report the AFM evaluation of the EBL patterning on several substrates; then we
4 discuss the AFM topography together with the optical Raman features of representative microscale NCA
5 assemblies.

6

7 3.1. Analysis of the Ordered Arrays

8 We considered four replicates of square arrays of wells (sectors) at varying d and Λ . Each lithographed
9 sector (**Fig. 2**) was identified with a capital letter depending on the couple (Λ , d). We analyzed the sample
10 surface by AFM after the lithographic process in order to compare the Computer Aided Design (CAD)
11 nominal characteristics of the template patterns with the actual ones. Representative AFM images of the
12 lithographic masks at two values of the area dose ($100 \mu\text{C}/\text{cm}^2$ and $20 \mu\text{C}/\text{cm}^2$) are shown in **Fig. 2**, the
13 experimental average d values are compared with the nominal ones in **Tab. 1**.

14 We did not find significant discrepancies between the nominal and measured Λ . Conversely, nominal and
15 experimental d values differed significantly for both doses (**Tab. 1**), and such differences increased at
16 smaller Λ . Moreover, at the higher doses, the correspondence between the actual and the nominal masks
17 was significantly deteriorated (see for example, the d values of the sectors with the higher Λ , A and B in
18 **Tab. 1**). In this respect, **Fig. 3** shows the AFM images and the corresponding height profiles
19 representatives of sectors A and B demonstrating the effect of the e-beam process on the thickness of the
20 Resist coating on silicon substrates. As shown in the AFM profiles of **Fig. 3b** and **Fig. 3c**, the e-beam
21 writing at the intense dose of $100 \mu\text{C}/\text{cm}^2$ resulted in symmetric wells, regularly disposed on the thin
22 resist film, although their effective d values resulted significantly larger than the nominal ones. In these
23 cases, the binding site of the NP is only the silicon surface exposed at the bottom of the well.

24 This effect of enlargement of the single site (named intraproximity) is due to the strong electron scattering
25 [23]. With decreasing Λ the scattering begins to affect the shape of the sites (interproximity effect) [23].

1 These effects cause an uneven degradation of the resist within individual sites as well as of the thickness
2 of the resist lithographed (compare the Resist thicknesses of Fig. 3a,b and c).

3 At fixed Λ (sectors A and B) a decrease of the nominal d by a factor of two, results in a dramatic
4 reduction of the difference between nominal and measured d . Since a shorter exposure time is needed to
5 write a smaller well, for the sectors designed at smaller d the electron scattering was consequently
6 reduced, and the mismatch between theoretical and measured parameters diminished. This could have
7 been expected, since the energy absorbed by the resist depends on both exposure time and e-beam
8 intensity, whose product defines the dose. The same considerations hold for the AFM analysis of the
9 sectors C and D, which are realized at Λ halved compared to A and B, respectively. At the higher dose,
10 the interproximity effect completely degraded the resist of the sector, so that only one single tank is
11 formed (see **Fig. 2**). The same happens for the sector (F,1) in which both Λ and d were halved by a factor
12 of two compared to (C,1) (**Tab. 1**).

13 In practice, because of the proximity effect, an empirical, dose-dependent threshold value could be
14 defined for the resist sinking, $RS_{\text{dose}} = \Lambda \cdot d$, below which we cannot solve individual NP binding areas
15 using EBL. At doses of $100 \mu\text{C}/\text{cm}^2$ RS_{100} is $\sim 0.5 \mu\text{m}$. At the dose value of $20 \mu\text{C}/\text{cm}^2$, RS_{20} is expected
16 to be smaller, and in fact we can get more densely structured arrays, (masks C and F, **Fig. 2**). The RS_{20}
17 value is $\sim 0.25 \mu\text{m}$.

18 However, to obtain smaller d the dose cannot be further reduced without risking that the area to be
19 excavated is not broken down completely. This is what happened in sector E: at dose $20 \mu\text{C}/\text{cm}^2$, the
20 AFM profilometry in **Fig. 4**, shows a large asymmetric degradation of the resist, partially overlapping the
21 area designed for NP functionalization. In these cases, it may be necessary to increase the dose by
22 increasing the exposure time (i.e. dwell time). In fact, by increasing the intensity of the e-beam the
23 measured average diameter is much larger, irregular (sector (E,1) in **Fig. 2**) and poorly reproducible.

24 This study shows that by properly adjusting the dose values very accurate and reproducible micro-
25 structured substrates can be prepared. Based on these results, we prepared the masks (A,1) (B,1) and

1 (B,2)* and used them as templates to successfully arrange long-range ordered micrometric and
2 submicrometric NP clusters, 2 and 10 micrometer spaced.

3 4 3.2. Analysis of the gold NCAs

5 The lithographic patterns were functionalized using two protocols based on either APTS/Glu/4-ATP or
6 MPTS linkers (see Section 2.2). After the NP deposition, and having lifted off the resist, we obtained a
7 regular 2D layout of NP clusters since the NPs are arranged only in the well binding sites (**Fig. 1**). The
8 AFM topography of the NCA of sectors A and B is shown in **Fig. 5**. In **Fig. 5a** the long range order is
9 acceptable, but apparently the number of NPs linked with the APTS—Glu—4-ATP is rather low.
10 Conversely, **Fig. 5b** shows that using MPTS linkers a regular array of densely packed NP clusters is
11 obtained. The AFM profiles on a representative single micrometric NP clusters of (B,1) after the binding
12 site being functionalized with 60 nm gold NPs through MPTS linker is reported in **Fig. 6a**. In the same
13 array the possible formation of an over layered excess of NPs is also shown in **Fig. 6b**. We cannot rule
14 out that the NP sometimes found stacked, forming multilayered clusters, did not come from the rare
15 presence of small aggregates of NP already present in the incubation solution, rather than being formed
16 by physisorption during the incubation process. Notably, we can instead exclude the presence of
17 impurities at atomic resolution as determined by AFM topography and the phase image (**Fig. 5b**). A
18 challenge still open it is to fine control the vertical organization of these NPs clusters.

19 The comparatively different NP binding yield we observe in **Fig.5a** and **Fig.5b** reflects the effect of
20 differing the number of steps and chemical involved in the two protocols of NCA fabrication protocols,
21 and, in turn a different anchoring agent concentration. Notably, the samples prepared by covalently
22 binding NPs via MPTS links are very stable, also in water for several days.

23 Among the advantages which influence the outcome of the functionalization, there could be the low
24 number of steps and chemicals involved in the protocols and the stability of the product: therefore the
25 protocol where it is involved the MPTS is favorable in this respect. Both the protocols have the vantage

1 of exposing a gold particle surface available to physi- or chemi-sorb different analytes although the tight
2 arrangement in two-dimensional clusters of the NP reduces the binding area portions available for
3 capturing the analytes. Alternatively, the overall gold NP surface could be engineered to bind the analytes
4 (e.g. proteins and cells) in solutions [26] and then captured by the arrays (e.g. APTS-Glu linkers) for the
5 microanalysis.

6 The potential of these NCA as sensitive Raman spectroscopy platforms was probed by following the
7 Raman signal of 4-ATP molecules localized onto the NPs surface. Herein we focused on the sector (A,1),
8 whose Λ resulted large enough to prevent any possible optical interferences and to optimize the
9 realization of spectroscopic mapping. The main results are shown in **Fig. 7**.

10 A representative Raman spectrum of a NP cluster of the array displaying $\Lambda = 10 \mu\text{m}$ and $d = 1 \mu\text{m}$
11 features, probed through the Raman porter 4-ATP is compared in **Fig. 7a** with the traditional Raman
12 spectrum of the same molecule (see Ref. [5] for the band assignment). As expected, the Raman cross-
13 section of 4-ATP when covalently linked to the NP clusters surface results strongly increased due the
14 SERS phenomenon [1,4]. The reason of the molecular spectroscopic signal enhancement is the surface
15 plasmon resonance of these gold nanostructures: the oscillation of the surface electron gas in the metal
16 nanostructure gives rise to a strong increase of the local electromagnetic field at the metal-dielectric
17 interface. For this reason, the spectral response of the molecules bound to the Np surface appears as if
18 they were illuminated by a much stronger field [1].

19 A reasonable way to evaluate the efficiency of a plasmonic substrate in signal enhancing is to calculate
20 the enhancement factor (EF), namely the ratio of SERS and Raman spectroscopic intensity per single
21 molecule. In our case, the spectroscopic intensity is obtained by integrating either the whole SERS
22 spectrum (overall EF) or the strong C-S stretching band of 4-ATP, centered at 1088 cm^{-1} in the Raman
23 spectrum and red-shifted to 1079 cm^{-1} in the SERS spectrum (band EF). The number of molecules
24 contributing to the spectroscopic signal is in both cases estimated via geometrical considerations (see [13]
25 for details). SERS signal amplification is known to benefit of two contributions: one electromagnetic,

1 arising from the substrate plasmonic resonance that enhances the local field around the molecules, and
2 one chemical, coming from the metallic substrate-molecule charge transfer. When considering the *overall*
3 enhancement factor, we are taking into account both the mechanisms. This EF estimate is more
4 appropriate for molecules covalently bound to the metal surface. On the other hand, the *band* EF is
5 expected slightly smaller, as we chose for the integration the C-S stretching band, which is known to be
6 enhanced only by electromagnetic mechanism: this can be considered representative for molecule
7 physisorbed to the metal surface. For this kind of substrates, as reported in **Fig. 7a**, we found an overall
8 EF of $\sim 1 \cdot 10^7$, which is quite notable when compared to the EF values reported in literature for gold based
9 substrates [15]. The strong intensity of the SERS C-S stretching band allowed us to spatially resolve the
10 presence of the clusters, and thus to find the full correspondence existing between the AFM topography
11 and SERS intensity maps. **Fig. 7b** shows indeed that the SERS intensity is displayed along the NP cluster
12 rows according to the periodicity of the array. Some significant drop or raise in SERS intensity ($>20\%$)
13 was detected and is related to the occurrence of isolated NPs assembly exhibiting uneven surface packing,
14 as confirmed both by optical inspection and AFM analysis (**Fig. 6b**). The large number of clusters per
15 $100 \times 100 \mu\text{m}^2$ area (100 clusters for the A sectors) enables to discard the worst data, thus ensuring a
16 contained variability of the SERS intensity, within roughly 20% ensembles up to 30 clusters, measured
17 consequently. At the best of our knowledge, it is not common to estimate the reproducibility of the
18 Raman signal reproducibility on plasmonic assemblies, and we believe that the result of an *overall* EF of
19 $(1.1 \pm 0.2) \cdot 10^7$, and of a *band* EF of $(0.30 \pm 0.06) \cdot 10^7$, is to be considered very positively [6,15]. The
20 latter result confirmed the previously mentioned idea that NPs clusters of micrometric and controlled
21 areas can provide quite regular, reproducible, and highly enhanced Raman signals.

22 Ultrasensitive detection technologies require the ability to integrate fast sensing, low sample and reagent
23 volumes, reduction of the size of equipment, possibility of portable devices and parallel operation for
24 multiple and automated analyses [26,27]. Within this challenge, the results presented herein, on the
25 possibility of realizing micrometric patches of closely packed NP over micrometric periodical inter-patch

1 distance, represents a further step toward the construction of efficient Lab-on-a-chip integrated systems
2 [27].

3

4 **4. Conclusions**

5 In this work we discussed the realization of accurate and reproducible e-beam lithographic patterns, that
6 have been exploited in order to isolate regularly-disposed areas on a Si substrate. We tested different
7 protocols of surface functionalization, used to induce the covalent self-assembled aggregation of gold
8 NPs. The characterization of the patterns was realized by AFM measurements, which showed the
9 presence of dense, highly packed NP clusters of micrometric size and spacing regularity. High and
10 reproducible optical signals displayed on the corresponding array periodicities were enlightened by
11 microRaman analysis. The demonstrated approach may be useful particularly in the aim of realizing
12 benchmark NCAs, featured as stable and reproducible gold NP clusters in the mesoscopic scale, leading
13 to the challenging production of improved opto- and conductive-microfluidic multiplex-sensing.

14

15 **References**

16 [1] J.N. Anker, W.P. Hall, O. Lyandres, N.C. Shah, J. Zhao, R.P. Van Duyne, Biosensing with plasmonic
17 nanosensors, *Nat. Mater.* 7 (2008) 442–453.

18

19 [2] M.P. Cecchini, V.A. Turek, J. Paget, A.A. Kornyshev, J.B. Edel, Self-assembled nanoparticle arrays
20 for multiphase trace analyte detection, *Nat. Mater.* 12 (2013) 165–171.

21

22 [3] B. Yan, S.V. Boriskina, B.M. Reinhard, Design and implementation of noble metal nanoparticle
23 cluster arrays for plasmon enhanced biosensing, *J. Phys. Chem. C* 115 (2011) 24437–24453.

24

1 [4] F. Domenici, A.R. Bizzarri, S. Cannistraro, Surface-enhanced Raman scattering detection of wild-type
2 and mutant p53 proteins at very low concentration in human serum, *Anal. Biochem.* 421 (2012) 9–15.

3
4 [5] F. Domenici, A.R. Bizzarri, S. Cannistraro, SERS-based nanobiosensing for ultrasensitive detection of
5 the p53 tumor suppressor, *Int. J. Nanomed.* 6 (2011) 2033–2042.

6
7 [6] B. Yan, S.V. Boriskina, B.M. Reinhard, Optimizing gold nanoparticle cluster configurations ($n \leq 7$)
8 for array applications, *J. Phys. Chem. C Nanomater. Interfaces* 115 (2011) 4578–4583.

9
10 [7] K. Saha, S.S. Agasti, C. Kim, X. Li, V.M. Rotello, Gold nanoparticles in chemical and biological
11 sensing, *Chem. Rev.* 112 (2012) 2739–2779.

12
13 [8] E. Boisselier, D. Astruc, Gold nanoparticles in nanomedicine: preparations, imaging, diagnostics,
14 therapies and toxicity, *Chem. Soc. Rev.* 38 (2009) 1759–1782.

15
16 [9] Y-C Yeh, B. Crerana, V.M. Rotello, Gold nanoparticles: preparation, properties, and applications in
17 bionanotechnology, *Nanoscale* 4 (2012) 1871–1880.

18
19 [10] P.K. Jain, X. Huang, I.H. El-Sayed, M.A. El-Sayed, Noble metals on the nanoscale: optical and
20 photothermal properties and some applications in imaging, sensing, biology, and medicine, *Acc. Chem.*
21 *Res.* 41 (2008) 1578–1586.

22
23 [11] E.S. Kooij, W. Ahmed, C. Hellenthal, H.J.W. Zandvliet, B. Poelsem, From nanorods to nanostars:
24 tuning the optical properties of gold nanoparticles, *Colloids and surfaces A.* 413 (2012) 231–238.

- 1 [12] S. Mühlig, D. Cialla, A. Cunningham, A. März, K. Weber, T. Bürgi, F. Lederer, C. Rockstuhl,
2 Stacked and tunable large-scale plasmonic nanoparticle arrays for surface-enhanced raman Spectroscopy,
3 J. Phys. Chem. C 118 (2014) 10230–10237.
- 4
- 5 [13] C. Fasolato, F. Domenici, S. Sennato, F. Mura, L. De Angelis, F. Luongo, F. Costantini, F. Bordi, P.
6 Postorino, Dimensional scale effects on surface enhanced Raman scattering efficiency of self-assembled
7 silver nanoparticle clusters, *Appl. Phys. Lett.* 105 (2014) 073105-1–073105-4.
- 8
- 9 [14] C. Fasolato, F. Domenici, F. Brasili, F. Mura, S. Sennato, L. De Angelis, E. Mazzi, F. Bordi, P.
10 Postorino, Self-assembled nanoparticle aggregates: organizing disorder for high performance surface-
11 enhanced spectroscopy, *AIP Conf. Proc.* 1667 (2015) 020012-1–020012-7.
- 12
- 13 [15] B. Yan, A. Thubagere, W.R. Premasiri, L.D. Ziegler, L. Dal Negro, B.M. Reinhard, Engineered
14 SERS substrates with multiscale signal enhancement: nanoparticle cluster arrays, *ACS Nano* 3 (2009)
15 1190–1202.
- 16
- 17 [16] M. Alba, N. Pazos-Perez, B. Vaz, P. Formentin, M. Tebbe, M.A. Correa-Duarte, P. Granero, J. Ferr-
18 Borrull, R. Alvarez, J. Pallares, A. Fery, A.R. de Lera, L.F. Marsal, R.A. Alvarez-Puebla, Macroscale
19 plasmonic substrates for highly sensitive Surface-Enhanced Raman Scattering, *Angew. Chem. Int. Ed.* 52
20 (2013) 6459–6463.
- 21
- 22 [17] I. Utke, S. Moshkalev, P. Russell (Eds.), Nanofabrication using focused ion and electron beams,
23 Principles and applications, Oxford University Press, Oxford, 2012.
- 24

- 1 [18] G.R. Brewer (Ed.), Electron-beam technology in microelectronic fabrication, Academic Press Inc.,
2 London, 1980.
3
- 4 [19] U.S. Tandon, W.S. Khokle, Patterning of material layers in submicron region, John Wiley & Sons,
5 New York, 1994.
6
- 7 [20] C.R.K. Marrian, D.M. Tennant, Nanofabrication, *J. Vac., Sci. Technol. A* 21 (2003) S207–S215.
8
- 9 [21] B.G. Prevo, D.M. Kuncicky, O.D. Velev, Engineered deposition of coatings from nano-and micro-
10 particles: A brief review of convective assembly at high volume fraction, *Colloids and Surfaces A:*
11 *Physicochemical and Engineering Aspects*, 311 (2007) 2–10.
12
- 13 [22] S.H. Kim, S.Y. Lee, S. M. Yang, G.R. Yi, Self-assembled colloidal structures for photonics. *NPG*
14 *Asia Mater*, 3 (2015) 25–33.
15
- 16 [23] S-F Hu, K-D Huang, Y-M Wan, C-L Sung, Proximity effect of electron beam lithography on single-
17 electron transistors, *Pramana J. Phys.* 67 (2006) 57–65.
18
- 19 [24] M.A. Mohammad, M. Muhammad, S. K. Dew, M. Stepanova, Fundamentals of electron beam
20 exposure and development, in: M. Stepanova, S. Dew (Eds.), Nanofabrication, Springer-Verlag, Wien,
21 2012.
22
- 23 [25] C.M. Halliwell, A.E.G. Cass, A factorial analysis of silanization conditions for the immobilization of
24 oligonucleotides on glass surfaces, *Anal. Chem.* 73 (2001) 2476–2483.
25

1 [26] C.P. Jia, X.Q. Zhong, B. Hua, M.Y. Liu, F.X. Jing, X.H. Lou, S.H. Yao, J.Q. Xiang, Q.H. Jin, J.L.
2 Zhao, Nano-ELISA for highly sensitive protein detection, *Biosens. Bioelectron.* 24 (2009) 2836–2841.

3

4 [27] F. Costantini, A. Nascetti, R. Scipinotti, F. Domenici, S. Sennato, L. Gazza, F. Bordi, N. Pogna, C.
5 Manetti, D. Caputo, G. de Cesare, On-chip detection of multiple serum antibodies against epitopes of
6 celiac disease by an array of amorphous silicon sensors, *RSC Adv.* 4 (2014) 2073–2080.

7

8

9

10

11

12

13

14

15

16

17

18

19

20

21

22

23

24

25

1 **Captions to figures**

2

3 **Fig. 1.** Schematic process flow of the template-assisted assembly of NCAs. After the developing process,
 4 the e-beam patterning (a) is followed by the functionalization of the exposed binding sites to allow the
 5 chemical bonding guided self-assembly of NPs (b); the lift-off process (c) leaves on the substrate the
 6 particles patches of diameter d with a periodical spacing Λ .

7

8 **Fig. 2.** The designed sectors arrangement template (four replicates for sector) together with the
 9 representative AFM topography of A, B, C, D, E, F sectors, lithographed using an area dose value of 100
 10 $\mu\text{C}/\text{cm}^2$ (row 1) and of 20 $\mu\text{C}/\text{cm}^2$ (row 2).

11

12 **Fig. 3.** AFM profiles to evaluate the thickness of the resist film after the spin-coating process (a), and
 13 after the e-beam process at dose of 100 $\mu\text{C}/\text{cm}^2$ on the sectors (A,1) and (B,1), corresponding to $\Lambda=10\ \mu\text{m}$
 14 (b) and $\Lambda=2\ \mu\text{m}$ (c). See also Tab. 1.

15

16 **Fig. 4.** AFM analysis of a part of the lithographed E sector ($\Lambda = 1\ \mu\text{m}$; $d = 0.125$) realized at e-beam dose
 17 20 $\mu\text{C}/\text{cm}^2$. The region between the red dashed lines indicates the resist area completely developed that
 18 can be functionalized effectively, much smaller than expected.

19

20 **Fig. 5.** AFM images of NCA obtained from A and B sectors using APTS+Glu+4-ATP (panel a) or MPTS
 21 (panel b) for linking the NPs onto the Si-OH binding sites.

22 Panel a, from left to right: the topography of array areas from (A,1) and (B,1) sectors specified in Tab.1,
 23 and the functionalization scheme.

24 Panel b, on the up side, from left to right: the topography of array portions of (A,1) and (B,1), and the
 25 Phase image of a representative NP cluster from (B,1); on the bottom side, from left to right: the three-

1 dimensional topography of an array portion from (B,2)* specified in Tab.1, the corresponding Phase
2 image, and the functionalization scheme.

3

4 **Fig. 6.** Nanoparticles cluster from sector (B,1), $\Lambda=2 \mu\text{m}$ and $d = 1 \mu\text{m}$, with three height profiles. The z-
5 values are in accordance with the overlap of several nanoparticles sized 60 nm, well compact with each
6 other to form discs to one (a) or sometimes even more layers of nanoparticles (b).

7

8 **Fig. 7.** Panel a: the SERS spectrum (red) of 4-ATP linked to the NP clusters, assembled on the
9 lithographed binding sites, is compared to the Raman spectrum (blue) of the 4-ATP Raman spectrum.
10 Both spectra are normalized to the number of molecules contributing to the spectroscopic signal (i.e.
11 present in the scattering volume). The Raman spectrum is multiplied by a scaling factor of 10^6 . The
12 integrated intensities used to estimate the enhancement factors are evidenced: the whole spectral integral
13 is coloured in light red (SERS) and light blue (Raman spectrum), while the area of the band centred at
14 1079 cm^{-1} (1088 cm^{-1} in Raman spectrum), estimated through a Lorentzian fitting, is evidenced with the
15 squared pattern in red and blue respectively. Panel b: a representative SERS intensity trend measured
16 along a row of the sector A ($\Lambda = 10 \mu\text{m}$, $d = 1 \mu\text{m}$), compared with the corresponding AFM topography.
17 Panel c: fast Fourier transform (FFT) obtained on AFM signal of sector A (upper plot, $|H(k)|$) is compared
18 to the FFT of the SERS signal on the same sector (lower plot, $|I(k)|$). The peak of the periodicity of 10
19 mm (centered at $0.1 \mu\text{m}^{-1}$) and the second harmonic (at $0.2 \mu\text{m}^{-1}$) are visible. The comparatively larger
20 width of the AFM FFT peaks is related to the different size of the frame measured (40 mm and 75 mm for
21 AFM and SERS acquisition, respectively).

22

Tab. 1. Geometric features of the sectors realized at variable e-beam dose. Standard deviations on the experimental d values are calculated on 5 profiles for each sector. The parameter Λ - d is critical for a successful design of the lithographic mask (see Section 3.1).

Sector	Dose value ($\mu\text{C}/\text{cm}^2$)	Λ (μm)	Nominal d (μm)	Λ - d (μm)	measured d (μm)
(A,1)	100	10	0.500	9.500	0.70 ± 0.06
(A,2)	20	10	0.250	9.750	0.25 ± 0.02
(A,2)*	20	10	0.50	9.500	0.44 ± 0.03
(B,1)	100	2	0.500	1.500	0.87 ± 0.07
(B,2)	20	2	0.250	1.750	0.30 ± 0.03
(B,2)*	20	2	0.50	1.500	0.57 ± 0.04
(C,1)	100	1	0.500	0.500^+	Bowl
(C,1)*	100	1	0.250	0.750	0.7 ± 0.1
(C,2)	20	1	0.250	0.750	0.33 ± 0.05
(D,1)	100	0.75	0.500	0.250	Bowl
(D,2)	20	0.75	0.500	0.250^{++}	Bowl
(D,2)*	20	0.75	0.250	0.500	0.23 ± 0.07
(E,1)	100	1	0.250	0.750	Not reproducible
(E,2)	20	1	0.125	0.850	0.040 (not uniform)
(F,1)	100	0.50	0.250	0.250	Bowl
(F,2)	20	0.50	0.125	0.375	0.040 (not uniform)

* Sectors with nominal d halved or doubled with respect to those shown in Fig. 2; $^+$ SR₁₀₀; $^{++}$ SR₂₀.

Figure 1

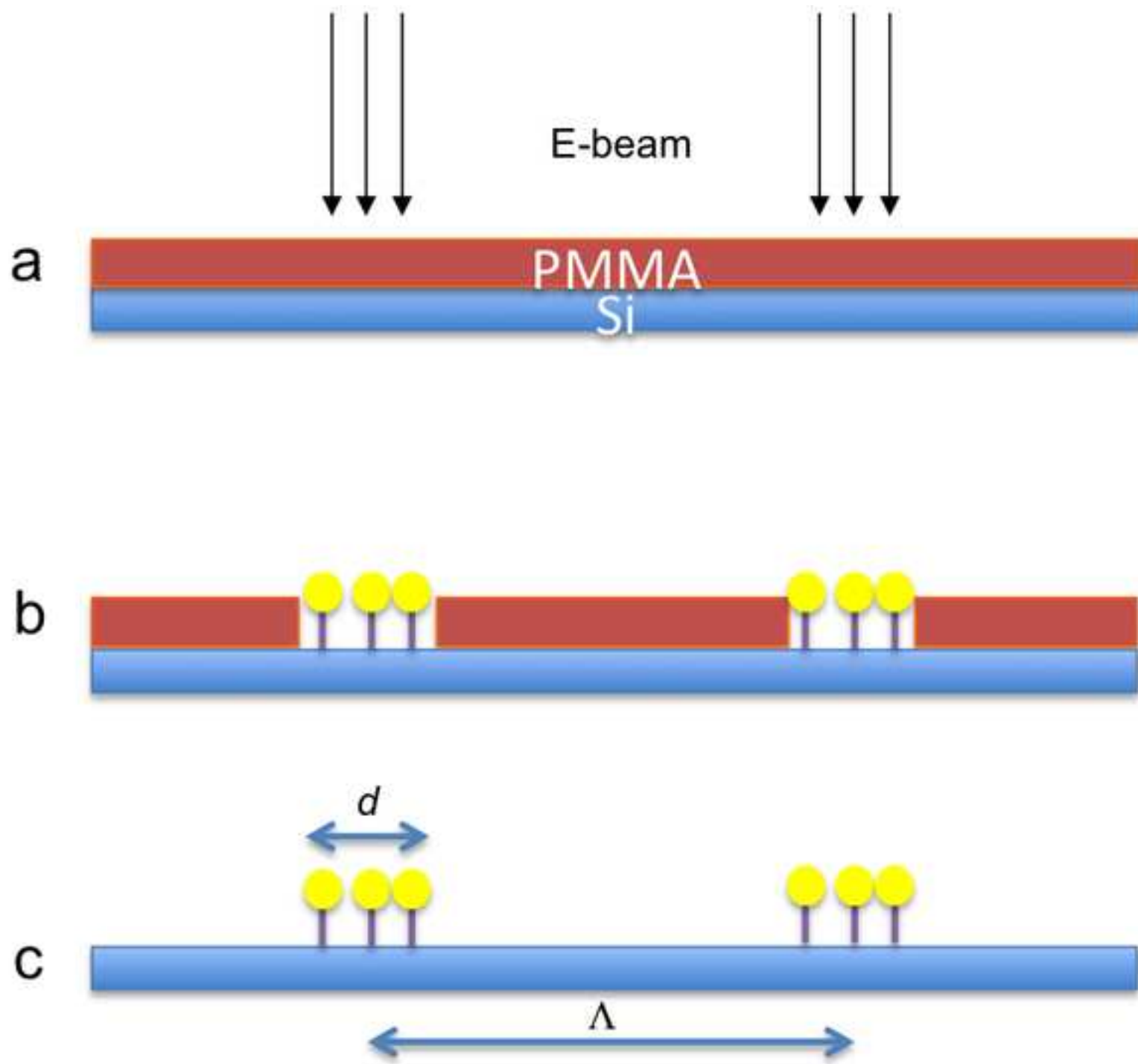


Figure 2

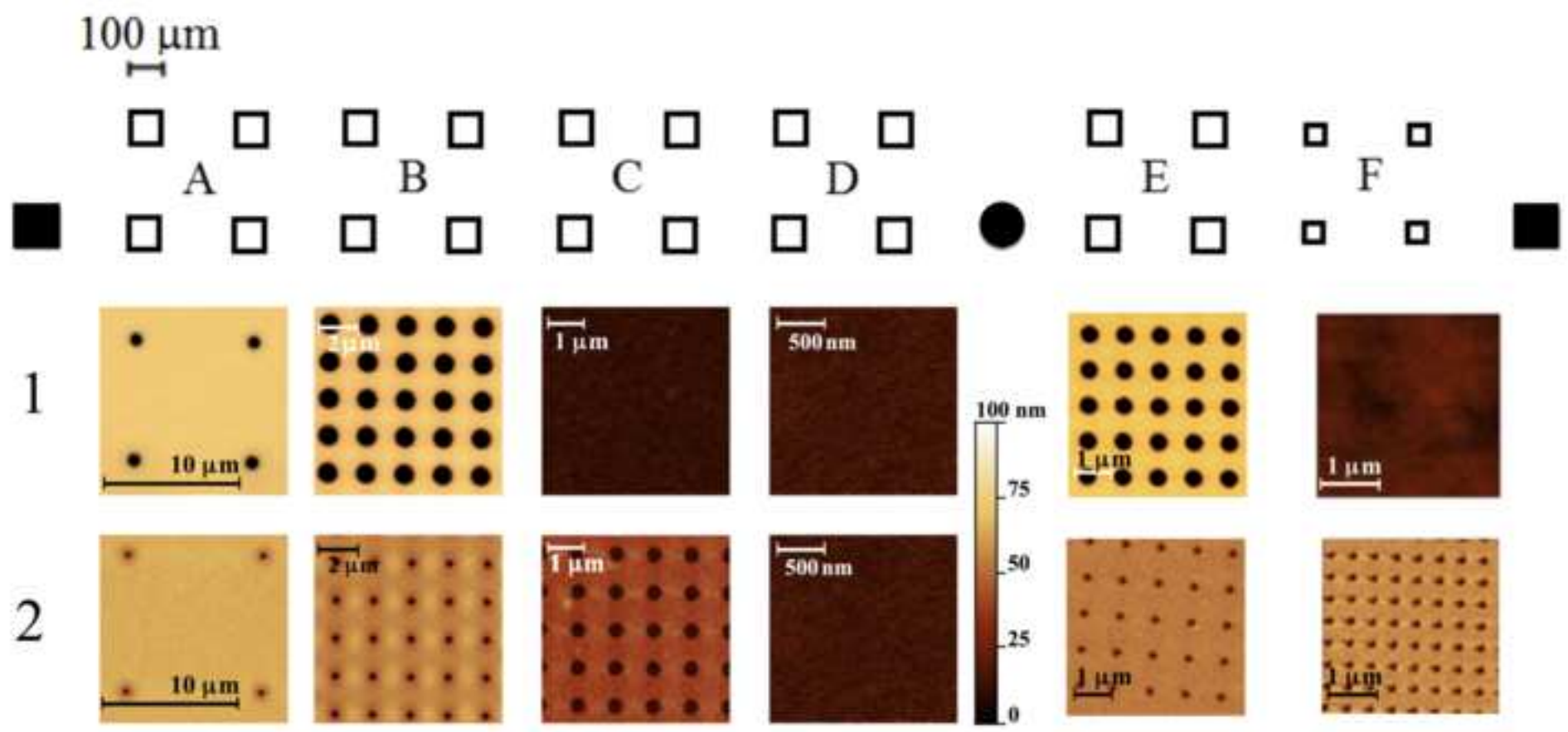


Figure 3

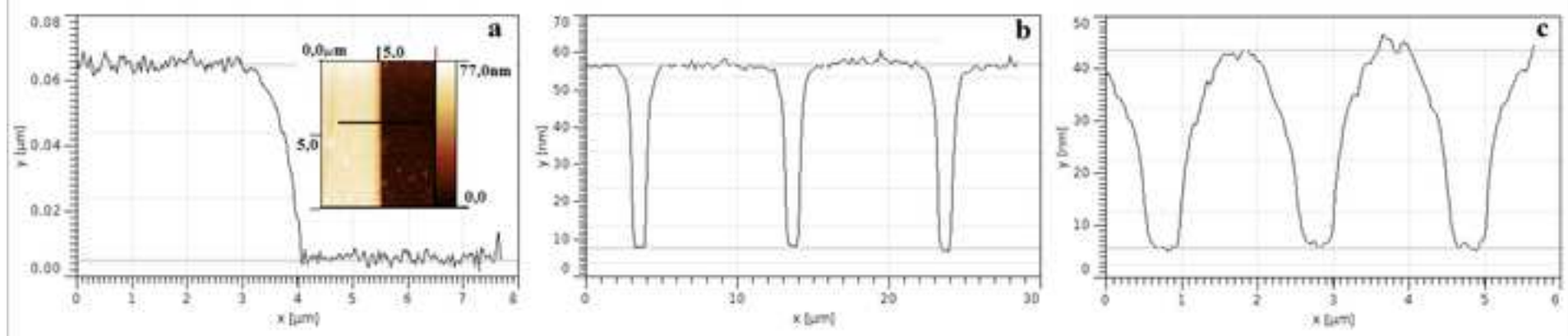
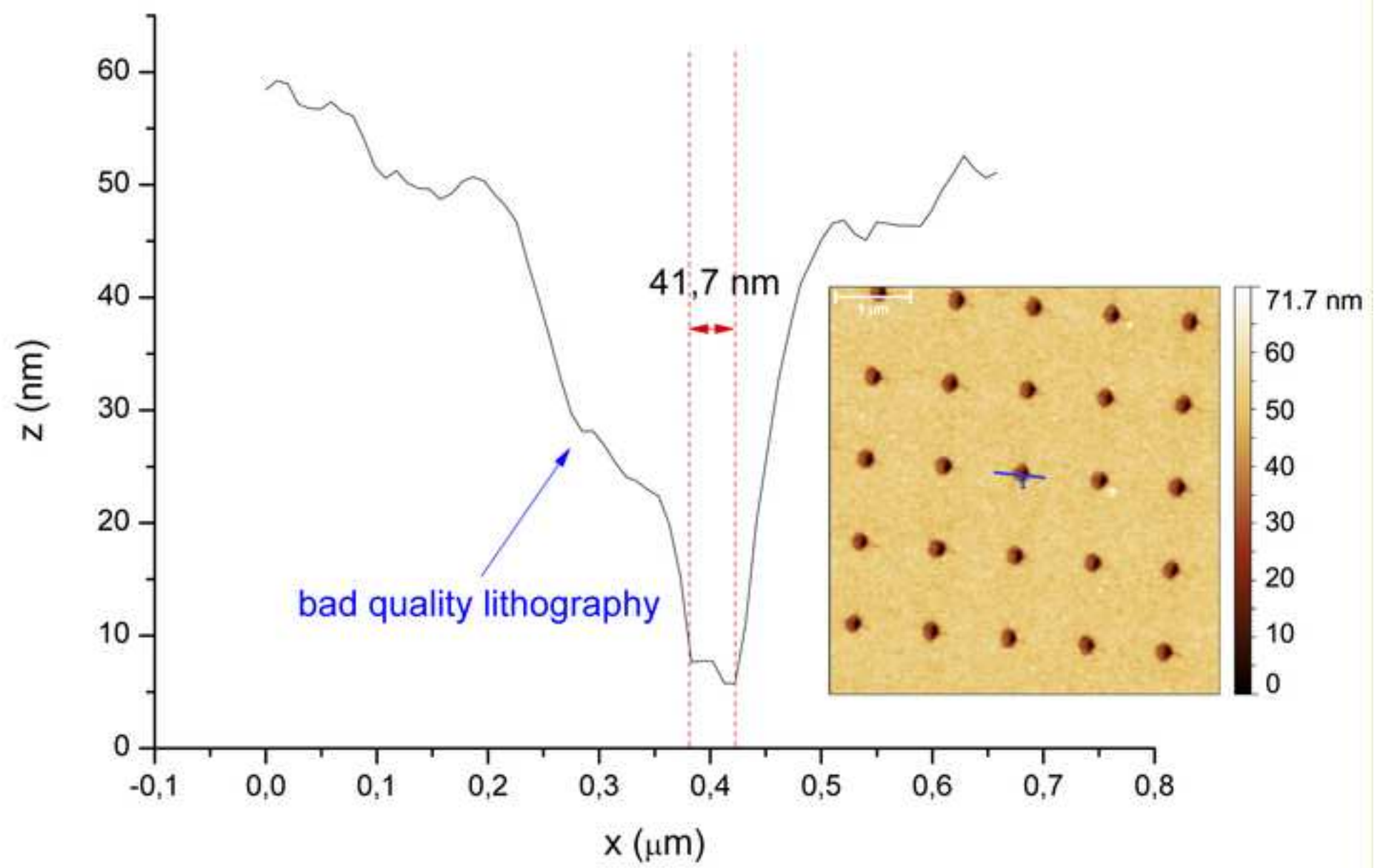


Figure 4



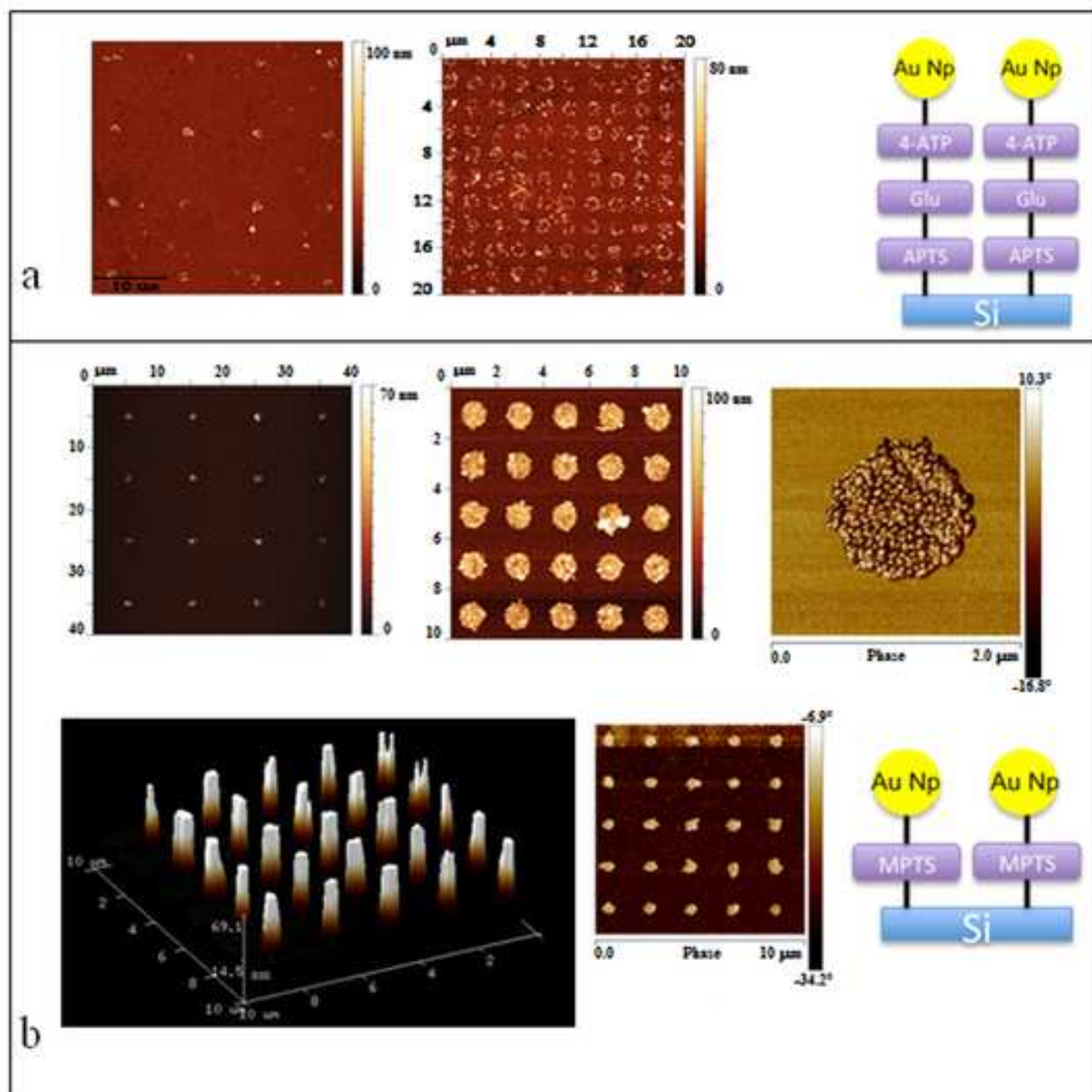


Figure 6

